JATIS Journal of Astronomical Telescopes, Instruments, and Systems

RESEARCH PAPER

Design, optimization, and simulation of a silicon pore optics-based X-ray interferometer

Aditya Garde,[a,*] Henk Hoevers,[b] Roland den Hartog,[b] Matthijs Langelaar,[a] Just Herder,[a] Luc Voruz,[c] Adam Lassise,[c] and Christian Körnig[c]

[a]TU Delft, Faculty of Mechanical Engineering, Precision and Microsystems Engineering, Delft, The Netherlands

[b]Space Research Organisation Netherlands, Leiden, The Netherlands

[c]cosine B.V., Sassenheim, The Netherlands

ABSTRACT. X-ray interferometry (XRI) is a promising technique for ultra-high resolution X-ray imaging. However, a major limitation of a regular design is the long length of the interferometer, which makes it virtually impossible to fit in a single spacecraft. The Willingale XRI design reduced the length by several orders of magnitude with the introduction of a slatted mirror. We propose to parallelize the interferometer using silicon pore optics (SPO). We show that SPO technology, currently being used to fabricate mirrors for ESA's upcoming NewAthena space mission, can be used for XRI and benefit by starting at a higher technology readiness level. We provide a detailed design description of Willingale XRI and combine it with SPO along with an optimization approach. Further, we apply the optimization approach for a Willingale's XRI testbed. The optimized design is checked with a ray optics simulation. Furthermore, we report successful fabrication of a slatted mirror manufacturing prototype. The optimized design and fabrication of a slatted mirror manufacturing prototype will serve as a first step toward building an XRI testbed for the demonstration of X-ray interference fringes that would demonstrate the feasibility of a Willingale type XRI.

 [DOI: 10.1117/1.JATIS.12.2.025001]

Keywords: X-ray optics; interferometry; ultra-flat mirrors; optimization; silicon pore optics

Paper 250197 received Nov. 10, 2025; revised Mar. 18, 2026; accepted Mar. 19, 2026; published Apr. 10, 2026.

1 Introduction

X-ray interferometry (XRI) is a promising technique with the potential for ultra-high resolution X-ray imaging,[1] advancing astrophysics into a fully new domain. The first step towards building an X-ray interferometer for space application was made by Cash et al.[2] in 2000. In this experiment, X-ray fringes were successfully demonstrated. However, the total length of the interferometer was ∼100 m for a baseline of 0.001 m. This is a problem because for a ultra-high resolution space instrument, which requires a baseline of 1 m, would require kilometers of length that cannot fit in a single spacecraft (∼20 m). To overcome this problem, Willingale in 2004 proposed a compact interferometer design[3] which introduced a slatted mirror, the X-ray equivalent of an optical beam combiner. This telephoto design reduced the length of the interferometer, which is driven by the ratio of the grazing angle and the beam angle and makes it possible to fit in a single spacecraft. In 2005, this design was successfully tested at visible wavelengths.[4] Further, in 2013 a prototype of the slatted mirror was fabricated but was not tested for X-ray interference fringes.[5]

*Address all correspondence to Aditya Garde, A.C.Garde@tudelft.nl

In 2020, den Hartog et al. proposed a Willingale interferometer for 1 keV and 7 keV testbeds.[6] Even though the design is feasible, it was not optimized and therefore left room for improvement. In the same year, Uttley et al. proposed an XRI mission concept and possible science cases, again based on the Willingale design.[7] In that paper, an interesting addition was made to the Willingale concept. It was suggested that the baselines could be stacked together to increase the collecting area of the interferometer. A common idea suggested as future work in both the aforementioned papers is an optimization to be carried out based on the slat size of the mirrors. In this paper, we formulate and carry out this optimization for maximizing the effective collecting area of the interferometer. In addition, the concept of stacking is included in the optimization loop.

A major practical challenge of stacking the baselines is the fabrication of a stacked slatted mirror. In this regard, Girou et al. in 2023,[8] hinted at the possible utilization of the industry ready silicon pore optics (SPO)[9] technology for X-ray interferometry. The adaptation of SPO from ESA's NewAthena[10] mission to X-ray interferometry is a natural progression, and we would start at a relatively high technology readiness level (TRL). In this paper, we show that it is possible to design a Willingale interferometer that satisfies the fabrication constraints of SPO. Further, we also demonstrate the practical feasibility by fabricating a prototype of the slatted mirror.

Elsewhere, there have been developments on other X-ray interferometer concepts. In 2023, Asakura et al.[11] experimentally demonstrated X-ray imaging using the Talbot effect. They demonstrated an angular resolution of 50 mas at 12.4 keV within a total interferometer length of 866.5 mm. The simplicity of the concept is impressive; however, the effective collecting area for such a concept would be very low. The dominant loss factor is the transmittance of the mask. In part II[12] of their two-part paper, they claim that the multipinhole system has a low transmittance of only 1.3%. The low transmittance due to its small opening fraction results in a low effective collecting area. Further, they improve the transmittance to 26% by replacing the multi-pinhole mask with multiple coded aperture masks. This alternative mask concept was tested experimentally at an angular resolution of 200 mas with a total interferometer length of 1.5 m. Even though there is improvement in the collecting area, a fundamental downside of this concept is that it works only for a specific wavelength. This is because the Talbot length at which the detector is placed is wavelength dependent. On the other hand, the Willingale design is a white light interferometer as fringes of all incident energies will form fringes at a given length of the interferometer. The detection of the fringes requires a sensor with a fine spatial resolution and sufficiently high energy resolution. Given the current sensor technology, fringes of lower energies can be resolved. However, detection of higher energy fringes is currently limited by the pixel size of the sensor as the fringe spacing decreases with an increase in energy.

A comparison of all the X-ray interferometer concepts is given in Table 1. The key performance metric for comparison is the angular resolution and the length of the interferometer. A small angular resolution and a small length are desirable. This can be quantified by comparing the product of the length and angular resolution. Clearly, the Willingale design is potentially capable of producing the highest angular resolution at a small length, and therefore, we investigate it in this paper.

The paper is organized as follows: first, we introduce the preliminaries of the Willingale design in Sec. 2. In Sec. 3, we show how the design can be parallelized along with how it can be fabricated by SPO. In Sec. 4, we propose the optimization problem formulation with an explanation of the objective function and constraints. A set of parameters is fixed at this stage for the demonstrator.

Table 1 Comparison of hitherto XRI designs. The Willingale design has the smallest length-angular resolution product, which means that it offers the best performance in a compact size.

XRI concepts	Energy (keV)	Length (m)	Angular resolution (mas)	Resolution × length (mas-m)	Status
Cash[2]	1.25	100	100	10000	Built and verified
Asakura 1: Multipinhole[13]	12.4	8.66	100	866	Built and verified
Asakura 2: Encoded masks[12]	12.4	1.5	200	300	Built and verified
Willingale design[6]	1.25	11.5	12.8	147.2	Under development

In Sec. 5, the design space of the problem is explored to show the optimal/design point. In Sec. 6, the optimal design is checked with a ray tracing simulation in COMSOL Multiphysics. In Sec. 7, we show successful fabrication of a slatted mirror manufacturing prototype with SPO technology. In Sec. 8, we draw conclusions from this design and analysis study along with future work.

2 Willingale Interferometer Design

In 2004, Willingale proposed a telephoto design,[3] which reduced the total length of the interferometer significantly. Figure 1 shows the schematic of the originally proposed Willingale design. The X-rays travel from left to right. The red and the green beams are the two arms of the interferometer. M1 and M3 are collector mirrors; M2 and M4 are combiner mirrors. The mirror M2 is a slatted mirror. The slatted mirror acts as a beam combiner of the two arms. The pair of red and green beams overlap at the detector to form interference fringes. A portion of the red beam goes through the gaps of the slatted mirror but does not contribute to fringe formation. This portion does not fall on the image plane and therefore does not contribute to the signal or the background of the interference fringes.

2.1 Slatted Mirror

The M2 mirror in the Willingale design is a special mirror that combines the beams of the two arms. Its purpose is transmitting one beam and reflecting the other beam. The reflective surface is called a slat, whereas the portion through which the corresponding beam is transmitted is called a gap. A slatted mirror may have multiple slat-gap pairs. Beams from each slat-gap pair completely overlap at the image plane to form interference fringes.

In the original Willingale design, the mirrors were assumed to be infinitely thin. Here, we consider the mirrors to have finite thickness. One of the consequences of the finite thickness of the slat is that it forms a shadow on the image plane. The overlap region at the image plane is therefore discontinuous. This results in a loss of fringes in the shadow of the slat thickness. A way to overcome this is to split the slatted mirror in two or more sections and stagger the slats to generate these missing fringes, as shown in Fig. 2.

In Fig. 2, the length of a slat and gap is given by l_{slat} and l_{gap}, respectively. The length of the M2 mirror is l_{m2}, and the length of the wafer required to cut out the slatted mirror is given by l'_{m2}. The depth of the mirror is given by d_m.

3 Parallelization of Willingale Interferometer

A key performance metric of an X-ray imaging instrument is the effective collecting area. Simulations of the interferometric reconstruction of AU Mic[7] show that larger counts result in a better image. In terms of a demonstrator, a large collecting area means faster fringe detection. For the Willingale design, the effective collecting area is primarily a combination of the surface

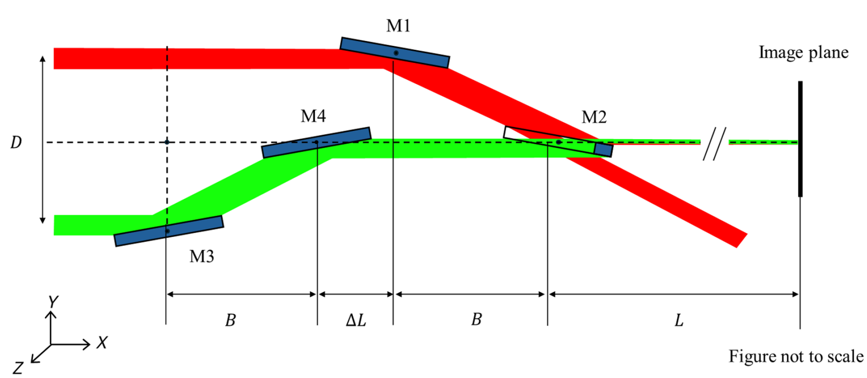

Fig. 1 Schematic of the Willingale interferometer[3] design made of four flat mirrors. The green and the red colored beams signify the two arms of the interferometer. The collector length is indicated by B and the combiner length is given by L. The two arms are separated by ΔL to avoid physical overlapping of the mirrors M1 and M4. The slatted mirror (M2) has only one slat to illustrate the function.

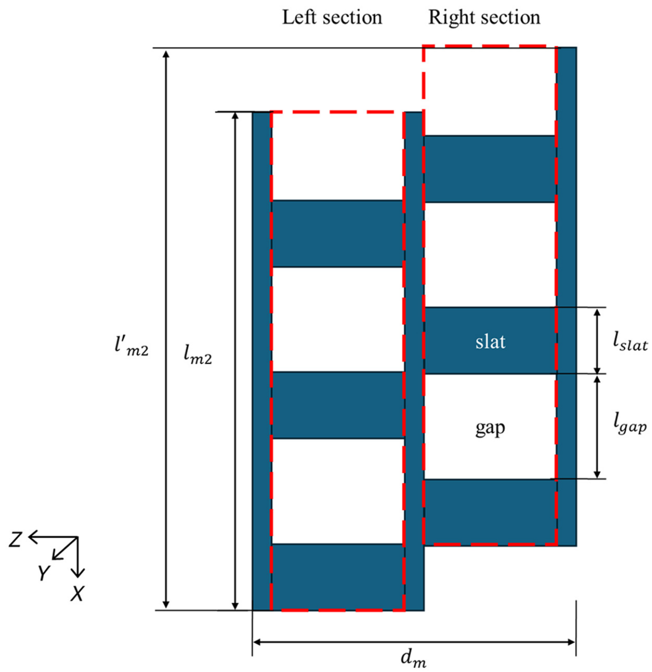

Fig. 2 Top view of a slatted mirror. The blue horizontal stripes are solid reflecting surfaces called slats, and the white horizontal stripes are rectangular holes called gaps. This mirror is partitioned into two sections. The slats in the left and right sections are staggered with respect to each other. This mirror has three slat-gap pairs in each section.

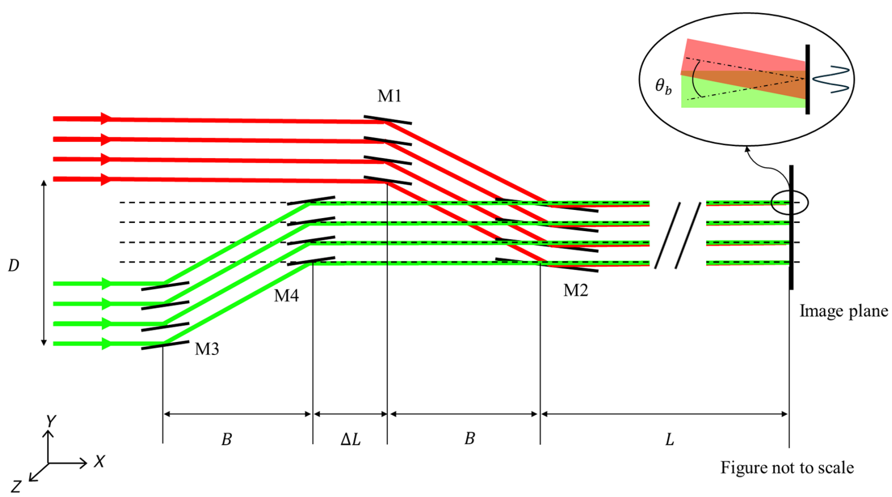

Fig. 3 Multiple baselines stacked on top of each other to form a parallelized XRI to increase the effective collecting area. The inset shows the two beams overlapping at a beam angle (θ_b) to form interference fringes. Mirror M2 needs to be misaligned by an angle $\frac{\theta_b}{2}$ to generate the beam angle.

area of the mirrors and their reflectivity, which in turn is a function of the grazing angle. An alternative way to increase the surface area of the mirrors is to stack the mirrors to create a parallel system of interferometers. Figure 3 shows each mirror unit with a stack of four mirrors. Each mirror in the stack forms an interferometer unit. Therefore, we have four sets of interferometer units with an identical baseline "D." As the design is a parallelized version of the Willingale design and as such, the optical path length equalization discussed in the Willingale[3] paper holds for each set of mirrors arranged in parallel.

3.1 Geometry of a Mirror Stack

Stacking the mirrors adds complexity to the design. For the purpose of deriving equations, we consider a stack of two flat mirrors as shown in Fig. 4. This geometry is applicable for M1, M3,

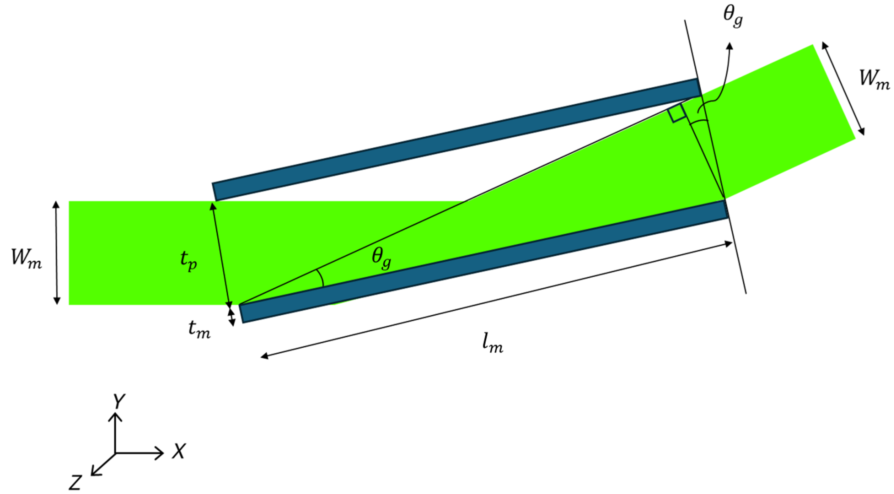

Fig. 4 Stack of two mirrors. The incoming and outgoing beams have identical beam widths (W_m). The wafer thickness is the sum of the pore thickness and the membrane thickness, that is $t_w = t_p + t_m$.

and M4 mirrors. To make efficient use of the reflecting surface, the incoming and outgoing beams should have identical beam width (W_s). This ensures that all the photons entering the mirror stack exit the stack without losses. The condition for incoming and outgoing beam widths to be identical is given by Eq. (1).

$$l_m = \frac{t_p}{\tan(\theta_g)}, \tag{1}$$

where l_m is the length of the mirror, t_p is the pore thickness and θ_g is the grazing angle of the mirrors.

A stack of slatted mirror needs careful consideration to have the reflected and transmitted beam width (W_s) equal. If we naively apply Eq. (1) to the stack of slatted mirrors, then we obtain one beam, which is larger than expected, as shown in Fig. 5(a). This happens because the membrane thickness (t_m) of the lower mirror transmits light.

The optimized geometry of a stack of slatted mirrors is shown in Fig. 5(b). Mathematically, this condition can be derived by equating the projected size of the wafer thickness to the size of the beams and the projected size of the membrane thickness. This can be seen in Fig. 6 for the case of two slats.

The generalized form for 'N_{slat}' number of slats is given by Eq. (2).

$$t_w \cdot \cos(\theta_g) = N_{\text{slat}} \cdot 2W_s + N_{\text{slat}} \cdot t_m \cdot \cos(\theta_g) \tag{2}$$

By rearranging and substituting for the beam width (W_s) as the projected size of the slats results in Eq. (3).

$$N_{\text{slat}} \cdot (2 \cdot l_{\text{slat}} \cdot \sin(\theta_g)) = (t_w - N_{\text{slat}} \cdot t_m) \cdot \cos(\theta_g) \tag{3}$$

Further, substituting the membrane thickness as a difference between wafer thickness and pore thickness results in Eq. (4).

$$2 \cdot N_{\text{slat}} \cdot l_{\text{slat}} \cdot \tan(\theta_g) = t_w - N_{\text{slat}} \cdot (t_w - t_p) \tag{4}$$

After some rearrangement, we can write Eq. (5). This equation sets the grazing angle in the XRI design.

$$\tan(\theta_g) = \left(\frac{t_p}{2} - \frac{t_w(N_{\text{slat}} - 1)}{2N_{\text{slat}}}\right) \cdot \frac{1}{l_{\text{slat}}} \tag{5}$$

Equation (5) can be simplified to Eq. (6). It is clear by comparing Eq. (6) with Eq. (1) that the length of the M2 mirror has to be larger than the other three mirrors.

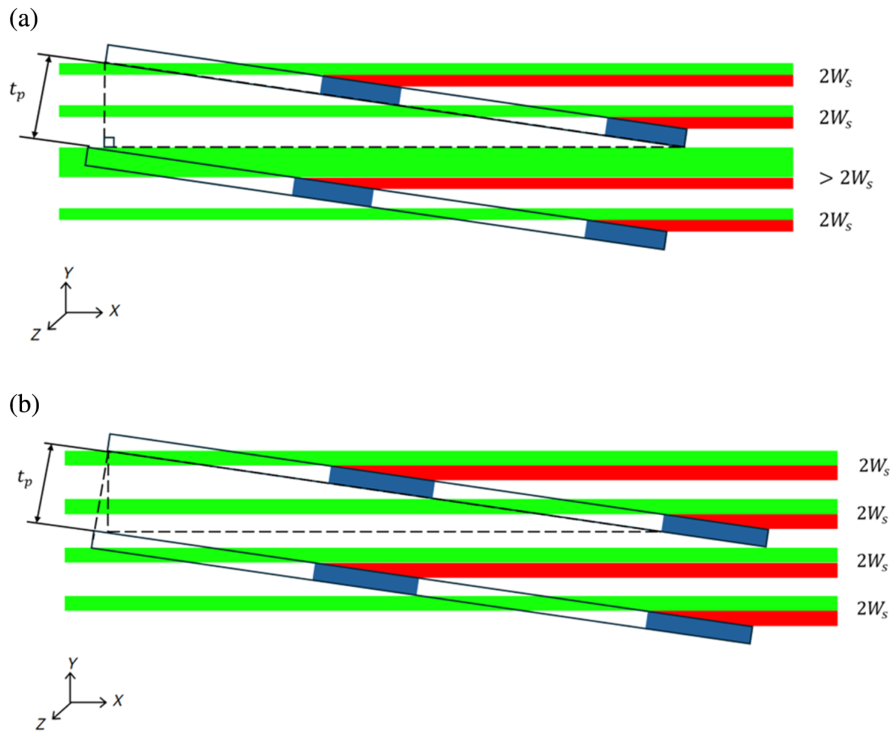

Fig. 5 (a) A stack of two slatted mirrors with two slats each. One of the transmitted beams has a beam width larger than expected. (b) Configuration of the slatted mirrors where the reflected (red) and transmitted (green) beams have identical width (W_s).

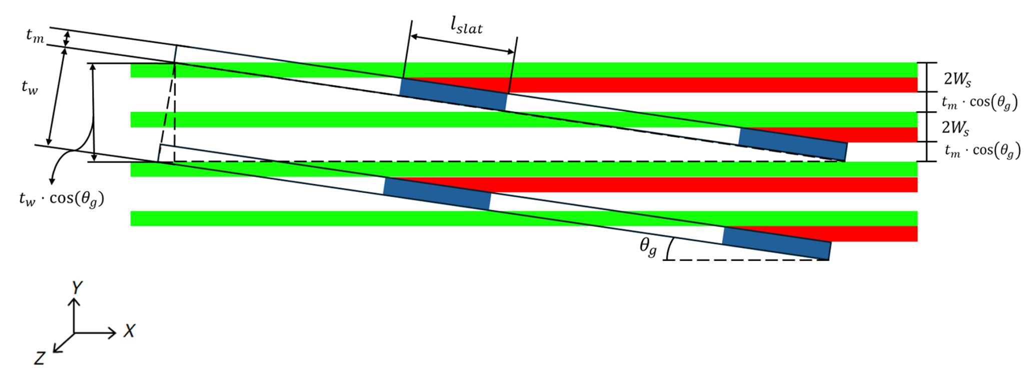

Fig. 6 Slatted mirrors with beam widths and the projected size of membrane thickness.

$$l_{m2} = \frac{t_w}{\tan(\theta_g)} \tag{6}$$

3.2 Fabrication of Parallelized Design

A key challenge is the fabrication of the parallel sets of mirrors because the individual mirrors need to be aligned with great precision. Each mirror would require a mechanism and an actuator, which would add to the complexity and cost. SPO[9] is based on a fabrication process used to produce stacks of X-ray mirrors, which falls in between the aforementioned alternatives. Further, this technology has been developed by the company cosine B.V. for ESA's NewAthena mission.[10] This process can potentially be adapted for XRI as the mirrors are flat and therefore easier to fabricate as compared with the curved mirrors used for NewAthena.

The envisioned fabrication process for a stack of flat mirrors is conceptually shown in Fig. 7 to introduce the parameters used in the following optimization. The basic idea of SPO is to stack a number of ribbed silicon wafers on top of each other. The space between the ribs form "pores," which let the light pass through the stacks. The nonribbed sides of the silicon wafers act as the reflecting surfaces. The wafer thickness is the sum of the pore height and membrane thickness.

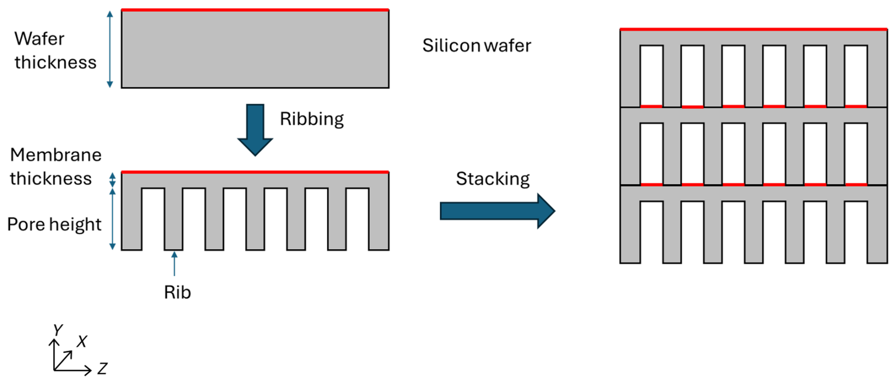

Fig. 7 SPO fabrication steps. The reflective surfaces are indicated in red.

Because the wafer thickness is well-defined and top and bottom surfaces are flat and unaffected by the ribbing, stacking does not compromise parallelism of the mirrors.

4 Optimization Problem Formulation

In this section, we propose an approach to maximize the XRI effective collecting area. All the relations for the design of the interferometer are laid out, by taking the practical constraints of SPO into account, to formulate an optimization problem.

4.1 Objective Function

The objective function of the interferometer design optimization is the effective collecting area of the interferometer. The effective collecting area is defined by Eq. (7).

$$A_{\text{eff}} = N_{\text{stack}} \cdot N_{\text{slat}} \cdot R^2(\theta_g) \cdot d_m \cdot l_{\text{slat}} \cdot \sin(\theta_g) \tag{7}$$

where N_{stack} is the number of mirrors in a stack, R is the reflectivity of the mirrors, d_m is the depth of the mirrors, l_{slat} is the length of the slat and θ_g is the grazing angle of the mirrors. The reflectivity is a nonlinear function of the grazing angle and photon energy.[14] Furthermore, it is squared because light is reflected twice in the interferometer. The depth of the mirror is driven by the size of the detector, which is 22 mm in our case. As a simplification, it is assumed that the complete mirror depth contributes to the collecting area, including the portion separating the sections of the slatted mirror. Further, analysis is required to determine the size of the separating portion.

4.2 Constraints

In this sub-section all the constraints applied in the optimization are motivated. In this formulation, we have four constraints in total.

4.2.1 *Constraint 1: length constraint*

The first constraint is on the total length of the interferometer. For the testbed, the maximum length of the interferometer is limited to 3.6 m, given the length of the laboratory space. The schematic of the interferometer is shown in Fig. 3, and total length can be calculated by Eq. (8).

$$L_{\text{tot}} = L + 2B + \Delta L \tag{8}$$

The total length is split into three parts: beam collector length B, arm separation length ΔL, and beam combiner length L.

The beam collector length (B) is a function of the baseline and the grazing angle:

$$B = \frac{D}{2 \cdot \tan(2\theta_g)}. \tag{9}$$

The arm separation length is the horizontal spacing required to prevent M1 and M4 from physically overlapping each other. It is modeled as the projection of the mirror on the optical axis. A factor of 1.2 is applied to have a safety margin.

$$\Delta L = 1.2 \cdot l_m \cos(\theta_g). \tag{10}$$

The combiner length is a function of the beam size per slat (W_s) and the beam angle (θ_b).

$$L = \frac{W_s}{\tan(\theta_b)}. \tag{11}$$

The combiner length can be expanded to arrive at Eq. (12).

$$L = \frac{l_{\text{slat}} \cdot \sin(\theta_g)}{\tan(\theta_b)}. \tag{12}$$

Here, it is evident that the slat size and grazing angle determine the combiner length. The beam angle is fixed by the fringe spacing, which is limited by the pixel size of the detector.

4.2.2 *Constraint 2: fringe constraint*

The second constraint is on the number of fringes per slat. A given slat size admits a particular number of fringes with a fixed fringe spacing. It is desirable to have more than one fringe per slat to detect fringes because the interferometer is vulnerable to the manufacturing errors and misalignment coupled with shadow regions due to the finite thickness of the slats, which may lead to difficulty in distinguishing neighboring dark bands in the fringes. Therefore, we set the minimum number of fringes per slat to a conservative value of 1.5.

The number of fringes per slat is given by Eq. (13).

$$N_{f/s} = \frac{L\lambda}{(\Delta y)^2}. \tag{13}$$

It is a function of the combiner length, wavelength of light λ and fringe spacing Δy.

4.2.3 *Constraint 3: stack height constraint*

The third constraint limits vertical spacing to prevent the two arms of the interferometer from overlapping with each other. This is modeled by ensuring that the tip of the M4 mirror does not overlap with M1. This is quantified by projecting half the length of the mirror stack on the baseline direction and limiting it to half the baseline, which is 5 mm. The projected thickness of a mirror stack (h) is given by the following equation:

$$h = t_{\text{stack}} \cdot \cos(\theta_g) + \frac{l_m}{2} \cdot \sin(\theta_g) \tag{14}$$

where the thickness of the mirror stack (t_{stack}) is given by,

$$t_{\text{stack}} = N_{\text{stack}} \cdot t_w \tag{15}$$

Equations (14) and (15) are based on the geometry of M4 mirror stack shown in Fig. 8.

4.2.4 *Constraint 4: mirror length constraint*

The fourth constraint is the maximum length of the mirror that can be fabricated. The maximum size of the mirror that cosine B.V. can currently produce is 110×54 mm^2. This constrains the maximum length to 110 mm.

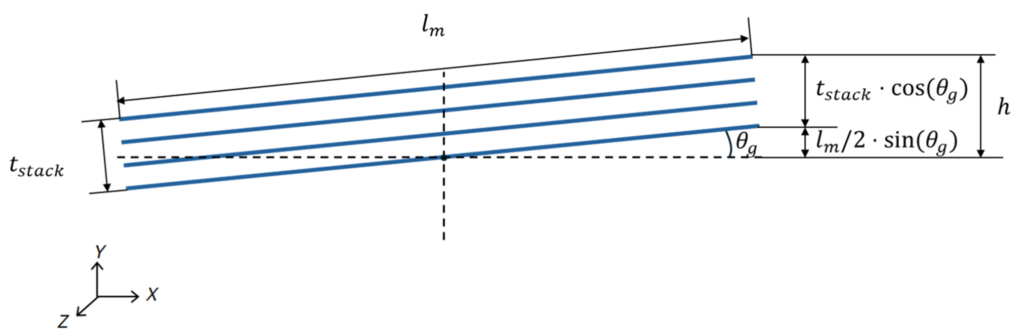

Fig. 8 Schematic of the cross-section of the M4 mirror stack. The projection of the mirror stack on the baseline is given by height *h*.

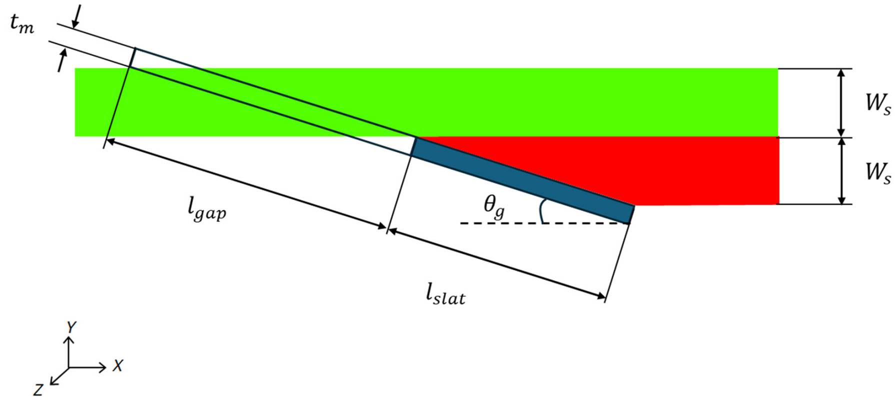

Fig. 9 Plate of slatted mirror in cross-section. The blue portion of the mirror is the reflecting surface, whereas the transparent portion is the gap. The green and red beams represent the transmitted and reflected beam, respectively.

The length of the M2 mirror can be seen from Fig. 2 and is defined by Eq. (16).

$$l'_{m2} = N_{\text{slat}} \cdot (l_{\text{slat}} + l_{\text{gap}}) + N_{\text{section}} \cdot l_{\text{slat}} \tag{16}$$

where N_{slat} is the number of slats, N_{section} is the number of sections in the slatted mirror, and l_{slat} and l_{gap} are the size of slats and gaps, respectively. Ideally, to make the size of the reflected and the transmitted beams identical, the gaps need to be larger than the slats. This difference in size can be seen in Fig. 9. The size of the gap, also seen in Figs. 5 and 6, can be calculated by Eq. (17).

$$l_{\text{gap}} = l_{\text{slat}} + \frac{t_m}{\tan(\theta_g)} \tag{17}$$

where t_m is the membrane thickness.

4.3 Problem Formulation

The discrete design variables are N_{stack}, N_{slat}, and the continuous design variables are slat length l_{slat} and pore thickness t_p. The optimization problem is presented in Eq. (18).

$$\begin{aligned}
&\max_x \; A_{\text{eff}} \\
&\text{s.t.} \; \frac{L_{\text{tot}}}{L_{\text{tot,max}}} - 1 \leq 0 \\
&\quad 1 - \frac{N_{f/s}}{N_{f/s,\text{min}}} \leq 0 \\
&\quad \frac{h}{h_{\text{max}}} - 1 \leq 0 \\
&\quad \frac{l'_{m2}}{l_{m2,\text{max}}} - 1 \leq 0 \\
&\quad x_{\text{min}} \leq x \leq x_{\text{max}} \\
&\quad x = [N_{\text{stack}}, N_{\text{slat}}, l_{\text{slat}}, t_p] \\
&\quad x_{\text{min}} = [1,1,1.5\ \text{mm}, 600\ \mu\text{rad}] \\
&\quad x_{\text{max}} = [7,4,15\ \text{mm}, 750\ \mu\text{rad}]
\end{aligned} \tag{18}$$

The constraint values for the testbed are stated in Table 2. Some of the parameters have to be fixed for the testbed from a practical point of view. These constants are provided in Table 3.

The size of the baseline is a practical choice because it dictates the length of the interferometer. The fringe spacing (Δy) is set by Nyquist sampling and is therefore driven by the pixel size of the camera. The mirror height is fixed to the depth of the camera sensor. The wafer thickness is determined by the current SPO activities at cosine B.V.

Table 2 Constraint values for the design of XRI demonstrator.

Quantity	Symbol	Value	Unit
Maximum interferometer length	$L_{\text{tot,max}}$	3.6	m
Minimum number of fringes per slat	$N_{f/s,\text{min}}$	1.5	—
Maximum stack height	h_{max}	5	mm
Maximum mirror size	$l_{m2,\text{max}}$	110	mm

Table 3 Constants for the design of XRI demonstrator.

Parameter	Symbol	Unit	Value
Baseline	D	mm	10
Energy	E	keV	1.25
Fringe spacing	Δy	μm	40
Wafer thickness	t_w	μm	775
Mirror depth	d_m	mm	20

5 Optimization

The optimization problem consists of two continuous design variables and two discrete design variables. The procedure to identify the optimum is a two-step process. First, various value combinations of the discrete design variables are tested to find the optimal combination of discrete design variables. Further, the design space is plotted to visualize the objective function and constraints to find the maximum value. The search led to a feasible configuration for $N_{\text{slat}} = 3$ and $N_{\text{stack}} = 6$ as shown in Fig. 10.

The plot shows the objective function increases non-linearly with increasing slat size and pore height. This is primarily because of the nonlinearity of the reflectivity curve. The feasible region is bounded by three constraints: g1, g2, and g4. The constraint g3 is a redundant constraint for this particular problem. It may become active for smaller baselines as the M1 and M4 mirrors come closer. As we want to maximize the objective function, the optimal point must lie on the g1

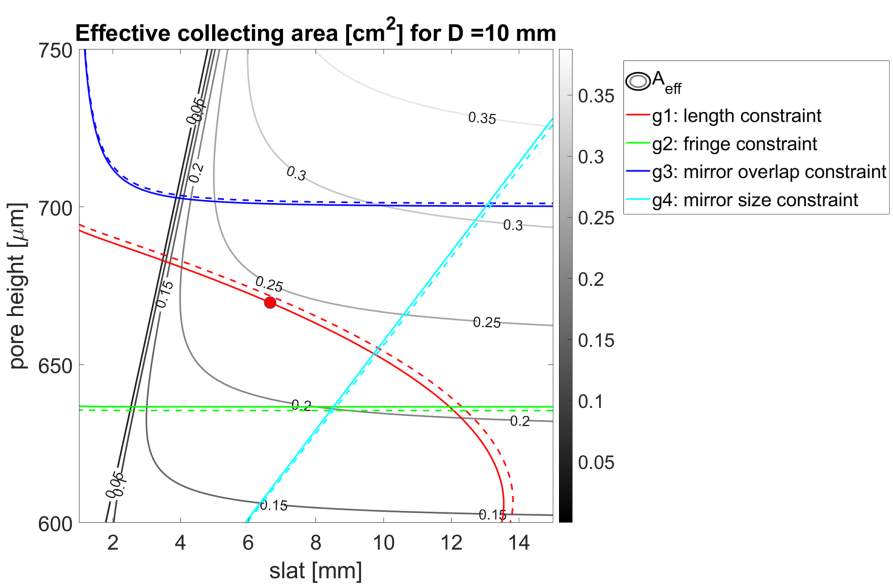

Fig. 10 Design space contour plot with constraints. The colorbar indicates the values of the effective collecting area in cm^2. The dashed lines indicate the infeasible side of the respective constraints.

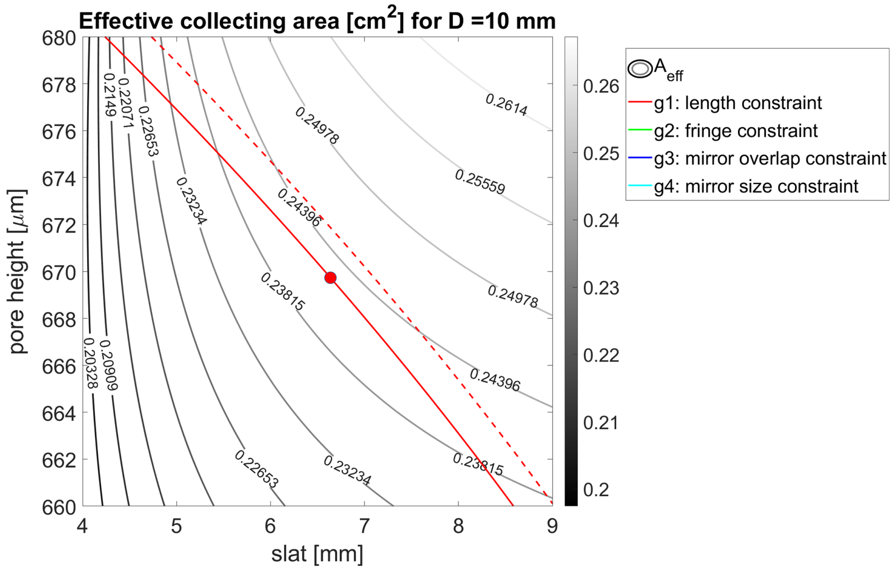

Fig. 11 Close-up of the contour plot near the g1 constraint. The maximum collecting area point lies at a pore height of 669.6 μm and a slat size of 6.63 mm and is indicated by the red dot.

constraint. This is seen in Fig. 11, which shows a close-up of the feasible region near the g2 constraint. The point with maximum collecting area lies at a pore height of 670 μm. However, cosine B.V. has its processing for NewAthena optimized for a pore height of 665 μm. Therefore, a pore height of 665 μm was selected, which has a minor loss of 2.2% in terms of effective collecting area.

All the design parameters for the chosen design point are given in Table 4. It is noteworthy that by building on the work of den Hartog,[6] which had a grazing angle of 2°, our optimization approach has a grazing angle of 0.56°, which reduces the total length of the XRI by a factor of 3 for the same baseline and a similar energy (1 keV).

6 Ray Tracing Simulation

A parametric ray tracing model has been developed such that it is scalable to different XRI designs. One of the key aspects of the design of XRI is to check the analytical design model with a ray tracing simulation. In this section, first, the purpose of the simulation is elaborated, followed by the setup of the simulation model in COMSOL Multiphysics. Finally, the simulation results are shown and analyzed.

6.1 Goal of the Simulation

The goal of the simulation is to check the following points:

1. Mirrors M1 and M4 do not overlap.
2. The size of the incoming and outgoing beams in all mirror stacks is identical.
3. The slatted mirror produces reflected and transmitted beams with equal beam widths.
4. The beams overlap at the required beam angle at the image plane.
5. The overlapping beams are identical in size.

6.2 COMSOL Model

The optical design geometry is built in COMSOL Multiphysics. The entire geometry is made parametric within the program to make the model scalable. This is done keeping the spacecraft design in mind, which will require multiple baselines spanning two orders of magnitude. There are two options within COMSOL to simulate optics, namely wave optics and ray optics. The wave optics module can also simulate the diffraction effects. The wave optics module requires the mesh size of the domain to be a fraction of the wavelength. In our case the size of the mesh would be a fraction of a nanometer over a length of 3.6 m. Such a model is computationally infeasible. On the other hand, the ray optics module is sufficient for the purpose of simulation. Therefore,

Table 4 Design parameters for a 10 mm baseline XRI.

Parameter	Symbol	Unit	Value
Energy	E	keV	1.25
Wavelength	λ	nm	0.992
Total length	L_{tot}	m	3.59
Baseline	D	mm	10
Equiv. angular res.	$\Delta\theta$	mas	10.23
Photon spatial resolution	Δp	μm	11
# Pixels per fringe	ppf	#	3.63
Grazing angle	θ_g	degree	0.561
Fringe spacing	Δy	μm	40
Beam angle	θ_b	μrad	24.8
Slat beam width	W_s	mm	74.1
# Fringes per slat	$N_{f/s}$	#	1.85
# Fringes per plate	$N_{f/p}$	#	5.56
Beam overlap length	L	m	2.99
Projected arm length	B	m	0.255
Arm separation length	ΔL	m	0.094
Focal length	F	km	0.403
M2 mirror length	l_{m2}	mm	79.14
M1, M3, and M4 mirror length	l_m	mm	67.92
Slat	l_{slat}	mm	7.57
Gap	l_{gap}	mm	18.8
Mirror reflectivity	R	#	0.942
No. of slats	N_{slat}	#	3
No. of plates in a stack	N_{stack}	#	6
Wafer thickness	t_w	μm	775
Pore thickness	t_p	μm	665.085
Effective collecting area	A_{eff}	m^2	2.389e-05

the ray optics module is used for modeling the optical design. The model setup is shown in Fig. 12. It shows the four stacks of mirrors. The side view shows the three sections staggered.

6.2.1 *Boundary conditions*

Two rectangular sources are added to represent the two arms of the interferometer. Each rectangular source comprises uniformly distributed point sources shooting rays parallel to the optical axis of the interferometer. The size of the sources corresponds to the projected size of a mirror unit section. Further, all the mirror surfaces are made perfect reflectors. In reality, there will be reflectivity losses, but this is not a point of interest for the purpose of this simulation. Furthermore, membrane sides facing the source are made perfectly absorbing. The surface of the M2 mirror separating the three sections is also treated as a perfect absorber. This is done to visualize the separation of the beams from its neighboring slat-gap pairs in cross section. In reality, these surfaces could be coated with an absorbing material to suppress reflection.

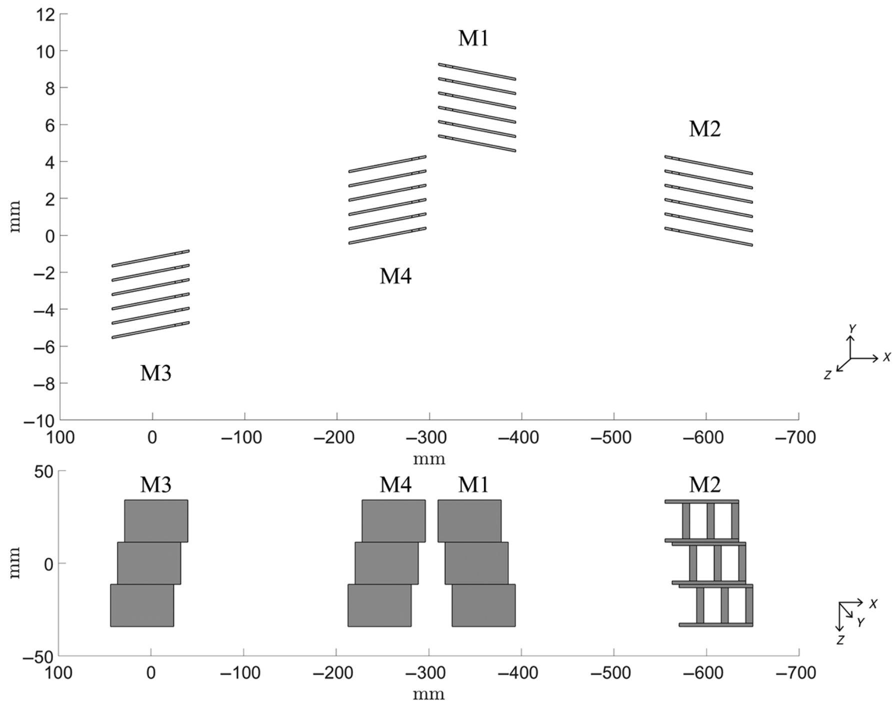

Fig. 12 XRI model built in COMSOL. The top panel shows the top view of the four mirror stacks. The bottom panel shows the side view of the mirror stacks. Note that the axis scales have been adjusted to generate a clear view of the mirrors.

6.2.2 *Results*

The results of the optical model are presented by zooming in on the relevant portions of the interferometer to show the required level of detail. First, the ray trace of the entire model is shown in Fig. 13. It is clear that the relevant beams end up on the image plane. Furthermore, a portion of the incoming beam passes through the slatted mirror away from the detector area.

Figure 14 shows that the M1 and M4 mirrors do not overlap. From closer inspection, it is clear that there is sufficient separation between the two mirror stacks. Therefore, point 1 has been checked.

The sizes of the reflected and transmitted beams were checked in COMSOL and were found to be of equal size, therefore, confirming points 3 and 4. Figure 15 shows a close-up of a set of beams at the image plane. Here beams from all three sections are simulated to show all sections produce equally sized beams.

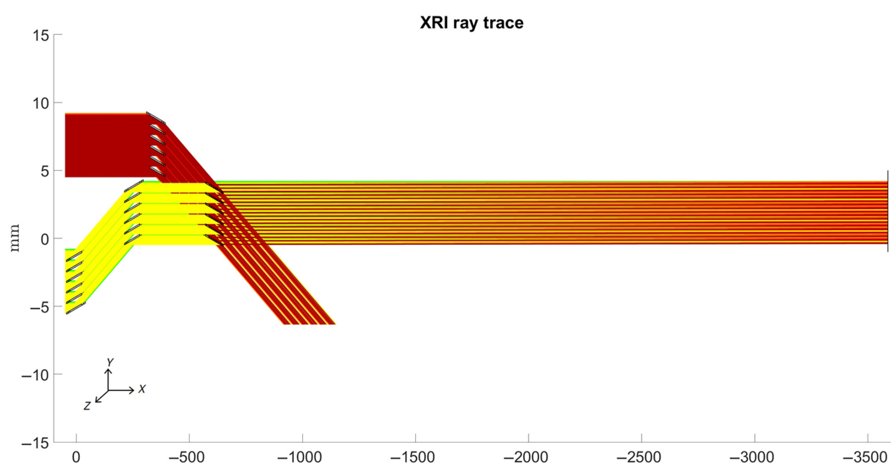

Fig. 13 Ray trace of XRI. The image is scaled down by a factor of 60 along the *x*-axis to make the mirrors and the beams distinguishable.

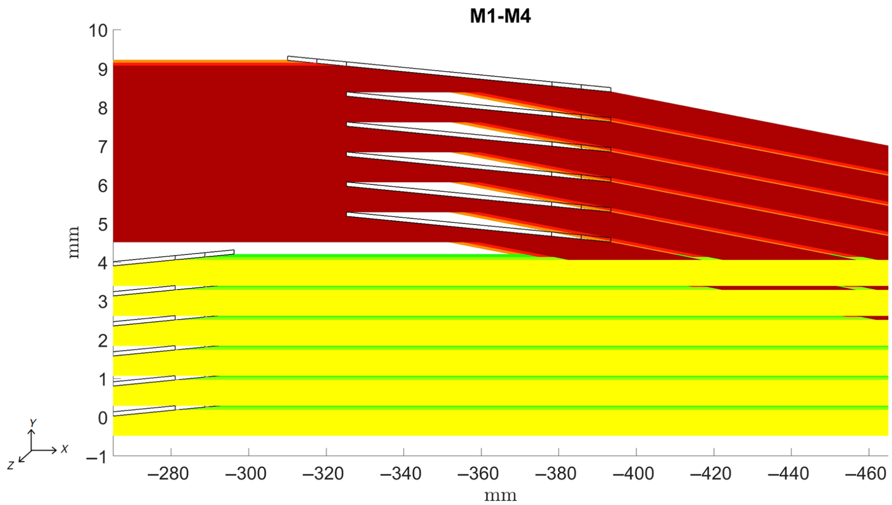

Fig. 14 Beam reflected by M4 mirror does not enter the M1 mirror.

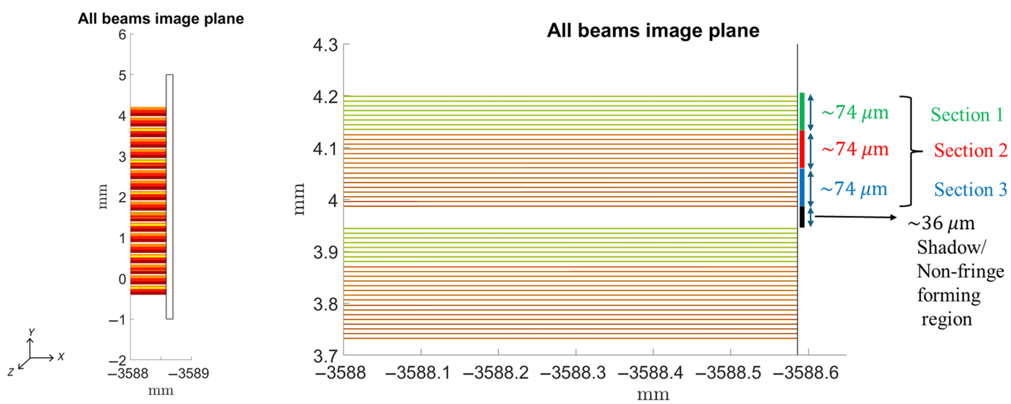

Fig. 15 Left panel shows a total of $N_{\text{slat}} \cdot N_{\text{section}} \cdot N_{\text{stack}} = 54$ fringe-forming beams at the image plane. Right panel shows two slat-gap beam pairs. The size of the beams from the three sections is 74 μm each as expected from Table 4.

Finally, Fig. 16 shows a close-up of the beams produced by a slat-gap pair. The beams transmitted through the gaps are horizontal, and the beams reflected by the slats arrive at an angle of 24.8 μrad.

7 Manufacturing Prototype

7.1 Requirements

There are two key requirements for the fabrication of XRI mirrors: (a) the surface figure and (b) parallelism of plates in a stack. The analytical equation to calculate the figure error required for a visibility of 90% has been previously derived by den Hartog et al.[6] The required surface figure for the optimized design is shown in Table 5.

There is a requirement for the parallelism of the mirror plates in a stack. Figure 17 illustrates the effect of an error $\delta\theta_p$ in the parallelism of one plate in a stack of two mirrors. For the path containing this plate and its counterpart in the other arm of the interferometer, it is no longer possible to fully overlap the beams at the location of the detector. As a consequence, non-coherent photons will appear on the detector above and below the fringes. Applying the requirement that due to these errors, not more than 10% of the coherent photons should be lost, we arrive at the following equation.

$$\delta\theta_p \leq \frac{n_f}{10} \cdot \frac{\Delta y}{L}. \tag{19}$$

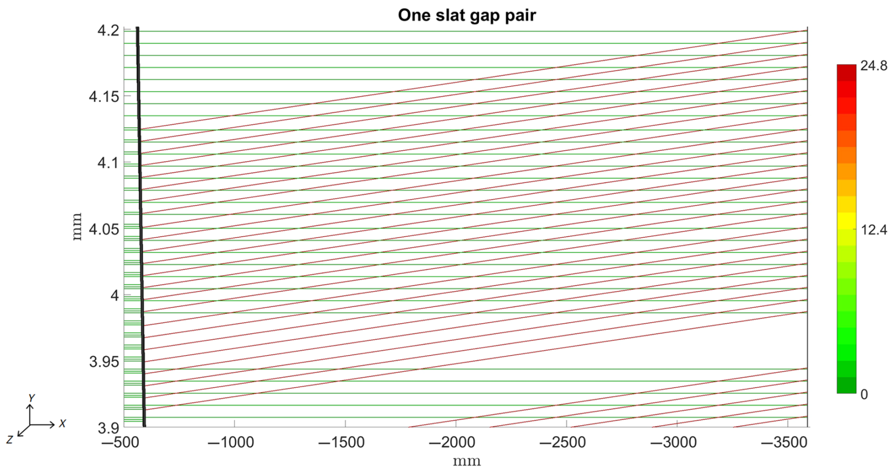

Fig. 16 Set of beams generated by one slat-gap pair overlapping at the image plane. The beam transmitted through the gaps (green) is perfectly horizontal, and the beam reflected (red) by the slat is at a beam angle of 24.8 μrad.

Table 5 Requirements for the optimized mirror design with grazing angle of 0.561 deg and photon energy of 1.25 keV.

Parameter	Symbol	Unit	Value
Maximum figure error	δs	nm	3.6
Maximum parallelism error	$\delta\theta_p$	μrad	2.46

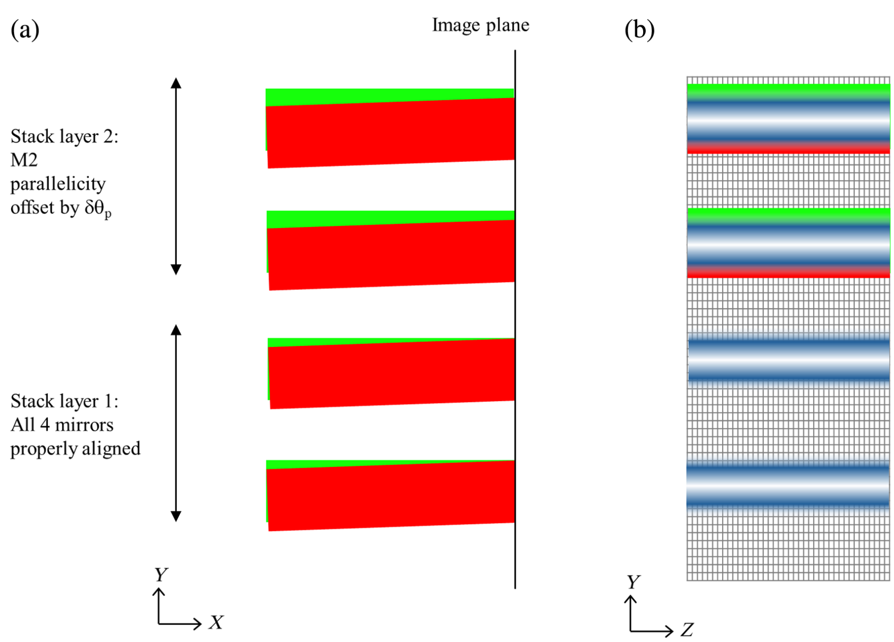

Fig. 17 Illustration of the effect of the rotation of one plate in a stack of otherwise parallel mirrors, highlighting the aspect of the red and green beams: their overlap at the location of the detector. Deviations from parallelism make it impossible to have all beams overlap simultaneously in all layers of the stack. This figure is a continuation of Fig. 6 toward the detector, assuming a slight tilt in the top plate, resulting in unmatched, i.e., noncoherent, photons above and below the interference pattern.

7.2 Prototype

In Sec. 3, we have shown that SPO is a promising route, building on the newAthena heritage, for the fabrication of the mirrors. To this end, we have designed and fabricated a manufacturing prototype of the slatted mirror at the cosine B.V. facility.

A slatted mirror plate was fabricated with the dimensions of the NewAthena row 1 plate[15] as shown in Fig. 18. In particular, the row 1 plate was used in this work as it was readily available for a manufacturing prototype, and its dimensions are closest to the optimized design. The slats were cut in the plate with a Laser MicroJet (LMJ) machine. The wafer survived the cutting process. Further, the slatted mirror was mounted on another wafer with direct bonding by hand. This was a first test of bonding, which will be replicated for stacking mirrors in the future. A limitation of stacking mirrors by hand is that the figure error exceeds the requirement. Flat stacking robots should be able to overcome this limitation.

The manufacturing prototype was successfully fabricated. The next challenges are to check if the slatted plates survive the stacking process, and if the stacking process, then can produce plates with the required surface figure.[16]

7.3 Status of SPO

SPO lends itself in a natural way to the massively parallelized implementation of Willingale design X-ray interferometers. Its development for the NewAthena mirrors is maturing, and an industrial-scale production line is set up over Europe to produce the 2.5 m mirror by 2032[17]. Already in 2022, a total half-energy width (HEW) below 8 arcsec over a significant fraction of the collecting area of a 34-plate module pair has been demonstrated, with 5 arcsec HEW over 10% of the area[17]. For the realization of XRI mirrors for a successor mission, the SPO technology offers huge advantages: Not only can parts of the production chain be re-used or re-purposed for the manufacturing of the XRI mirror modules, but there is also the expertise gained with the development of a high-TRL SPO mirror with a collecting area comparable to what is needed for an XRI successor mission, which has been build up by cosine B.V. over the past two decades and which is unparalleled by any other mirror technology.

Development is needed at cosine B.V. for meeting the requirements of XRI. Specifically, the surface figure and parallelism of the mirrors require attention. The current measurements do not allow us to measure the surface figure with required precision. For meeting the parallelicsm requirement, the current stacking process which is at 8 arcsec is an order of magnitude away from the XRI requirement of 0.5 arcsec calculated in Table 5. Although, it must be noted that the current stacking process uses curved mirror instead of flat mirrors required for XRI. We expect to have more insights after cosine B.V. has done stacking of flat plates.

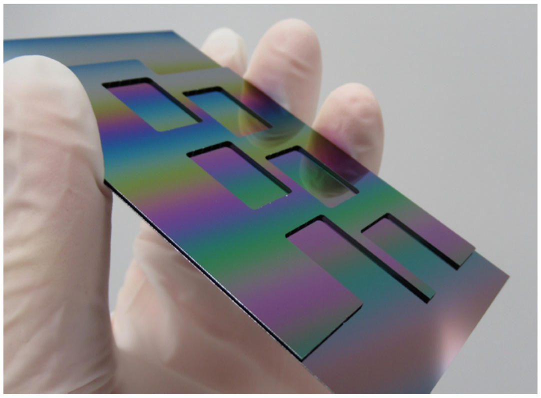

Fig. 18 First manufacturing prototype of the realized slatted mirror mounted on a wafer. The gaps (c.f. Fig. 2) in the slatted mirror, expose the wafer on which it is bonded. A functional prototype of the optimized configuration will require a stack of six slatted mirrors.

8 Conclusion and Future Work

We have provided a detailed design method for the Willingale XRI with SPO. The SPO uses a stack of mirrors, increasing the effective collecting area of the interferometer. An optimization problem was formulated to maximize the effective collecting area. In addition, critical geometrical and fabrication constraints were identified and formulated. This formulation can be used for future laboratory demonstrators as well as space instruments. The optimization approach was used to design a laboratory testbed with a baseline of 1 cm and a length of 3.6 m.

The functionality of the optical design was checked with a ray tracing simulation. The optical design within the simulation program was made fully parametric to enable testing of different baselines in the future. This is vital because the envisioned space instrument will consist of multiple baselines.

Finally, a slatted mirror manufacturing prototype was successfully fabricated at cosine B.V. to demonstrate practical feasibility. In a larger context, we have shown that SPO, a process developed at an industrial scale for ESA's upcoming NewAthena mission, is a strong candidate for X-ray interferometry. Overall, we have made a big step toward the realization of X-ray interferometer optics as we move closer to the next generation of X-ray space observatories.

Given the findings of this study, there remain a few challenges to be worked out. The major challenge is achieving the proper surface figure of the mirrors and the parallelism of mirrors in a stack. Further, the stacking of the slatted mirror is seen as a challenge given its fragility. The bridge between design and realization of the mirror stacks is a significant challenge and is under co-development with cosine B.V.

Disclosures

The authors declare that there are no financial interests, commercial affiliations, or other potential conflicts of interest that could have influenced the objectivity of this research or the writing of this paper.

Code and Data Availability

Data sharing is not applicable.

Acknowledgments

The authors would like to acknowledge discussions with Phil Uttley regarding the design of mirrors not only for the testbed but also for the future spacecraft from a science case perspective. The authors would also like to thank Richard Willingale for his useful comments during the XRI workshop. This work was supported by the Dutch Research Council (NWO) under Grant No. NWOI – 23.0865.

References

1. P. Uttley et al., "The high energy universe at ultra-high resolution: the power and promise of x-ray interferometry," *Exp. Astron.* **51**, 1081–1107 (2021).
2. W. Cash et al., "Laboratory detection of x-ray fringes with a grazing-incidence interferometer," *Nature* **407**, 160–162 (2000).
3. R. Willingale, "A practical system for x-ray interferometry," *Proc. SPIE* **5488**, 581–592 (2004).
4. R. Willingale, G. Butcher, and T. J. Stevenson, "Optical demonstration of an x-ray interferometer," *Proc. SPIE* **5900**, 59001G (2005).
5. R. Willingale et al., "A slatted mirror for an x-ray interferometer manufactured in silicon," *Proc. SPIE* **8861**, 88611S (2013).
6. R. den Hartog et al., "The development of a testbed for the x-ray interferometry mission," *Proc. SPIE* **11444**, 114447W (2020).
7. P. Uttley et al., "An x-ray interferometry concept for the ESA Voyage 2050 programme," *Proc. SPIE* **11444**, 114441E (2020).
8. D. Girou et al., "Silicon pore optics: a mature and adaptable x-ray mirror technology," *Proc. SPIE* **12679**, 1267905 (2023).
9. M. J. Collon et al., "Status of the silicon pore optics technology," *Proc. SPIE* **11119**, 111190L (2019).
10. M. Bavdaz et al., "NewATHENA optics technology," *Proc. SPIE* **12679**, 1267902 (2023).
11. K. Asakura et al., "Multi-image x-ray interferometer module: I. Design concept and proof-of-concept experiments with fine-pitch slits," *J. Astron. Telesc. Instrum. Syst.* **9**(2), 025004 (2023).

12. K. Asakura et al., "Multi-image X-ray interferometer module: II. Demonstration of high-resolution X-ray imaging with regular-interval coded apertures," *J. Astron. Telesc. Instrum. Syst.* **10**(4), 045002 (2024).
13. K. Asakura et al., "Subsub-arcseconds x-ray imaging with multi-image x-ray interferometer module (MIXIM): experimental results," *Proc. SPIE* **11444**, 114441D (2020).
14. E. Gullikson, "Mirror reflectivity," https://henke.lbl.gov/optical_constants/mirror2.html (accessed 22 October 2025).
15. M. Bavdaz et al., "The NewAthena x-ray optics," *Proc. SPIE* **13626**, 1362602 (2025).
16. A. F. Shipley and W. C. Cash, "Alignment of a grazing incidence x-ray interferometer," *Proc. SPIE* **4444**, 17–28 (2001).
17. M. Collon et al., "The development of the mirror for the Athena X-ray mission," *Proc. SPIE* **12777**, 127770R (2023).

Aditya Garde is a PhD candidate at TU Delft in the department of precision and microsystems engineering. He received his MSc degree in mechanical engineering from TU Delft in 2022. His current research interests include X-ray optics, optimization, and precision mechanisms.

Biographies of the other authors are not available.